Synchronized Switch Harvesting on ElectroMagnetic System: a nonlinear technique for hybrid energy harvesting based on active inductance

Mickaël Null Lallart, Giulia Lombardi

Synchronized Switch Harvesting on ElectroMagnetic System: a nonlinear technique for hybrid energy harvesting based on active inductance

Mickaël LALLART[1,*] and Giulia LOMBARDI[1]

[1] *Univ. Lyon, INSA-Lyon, LGEF, EA682, F-69621, VILLEURBANNE, FRANCE*

Abstract

This paper proposes a hybrid nonlinear interface combining both piezoelectric and electromagnetic effects for energy harvesting purposes. Based on the previously developed Synchronized Switch Harvesting on Inductor (SSHI) scheme, this technique aims at including as much as electroactive parts as possible, thus advantageously replacing the passive inductance in the SSHI approach by an electromagnetic transducer. The proposed scheme, called Synchronized Switch Harvesting on ElectroMagnetic system (SSH-EM) results in a significant increase of the output voltage, thus leading to a consequential increase of the harvested power, especially in the case of low-coupled systems, when compared to the classical SSHI approach and the standard approach (*i.e.*, directly connecting the piezoelectric element to the load through a diode bridge rectifier and a smoothing capacitor). The working principle, along with theoretical developments, and the supporting experimental results, are presented, both considering structures featuring constant displacement magnitude or structures driven at their resonance frequency with a constant excitation magnitude.

Keywords: Vibrational hybrid energy harvesting, piezoelectric, electromagnetic, synchronized switch, nonlinear circuit

1. Introduction

The development of wireless sensor networks has received a great deal of interest in research communities over the past two decades [1, 2, 3]. Simultaneously, advancements in low power electronic design and fabrication have drastically reduced the power consumption of small electronic devices opening the possibility for autonomous sensor nodes and, more particularly, in the framework of "Internet of Things" [4]. These sensors are in most cases alimented by conventional batteries which, however, show limitations in terms of ageing phenomenon (self-discharge), whether the battery is used or not, limiting the battery applications, particularly when exposed to relatively harsh environment conditions and/or when placed in confined and hardly accessible locations [5]. Hence, harvesting ambient energy to supply such sensor nodes appears to be a key technology in

---

*Corresponding author - mickael.lallart@insa-lyon.fr

order to replace the role of such batteries and go towards the development of autonomous self-powered devices [6]. When dealing with energy harvesting from the nearby environment, several sources can be considered; radiations, thermal gradients and vibrations are just few examples [7]. Among these, the strong ubiquity and the high power density of mechanical vibrations make these an interesting potential power source for electromechanical systems [8, 9]. Converting the mechanical energy from ambient vibrations into electrical energy is performed by a transducer. Among the existing ones, piezoelectric [10, 11, 12, 13, 14, 15] and electromagnetic [16, 17, 18, 19] energy harvesters have received much attention, as they both can reach relatively high power levels with no external voltage source requirement.

Piezoelectric energy harvesters, based on the direct piezoelectric effect, have been widely studied and nonlinear electronic treatments (*i.e.* adding a nonlinear element to the circuit, such as switch, as opposite to linear case - which usually consists of a linear load, such as a resistance, connected to the transducer) applied to the piezovoltage have been developed in order to enhance the efficiency of the energy conversion [20, 21, 22]. For instance, Guyomar *et al.* proposed a simple but original treatment, namely the SSHI (Synchronized Switch Harvesting on Inductor), for greatly improving the energy conversion abilities of piezoelectric materials [23], resulting to a typical gain factor of 8 in terms of harvested energy in comparison to the classical approach. In order to further increase the conversion abilities of piezoelectric elements, several techniques derived from this method have been successively proposed, although introducing further complexity to the circuit [24, 25, 26, 27].

Electromagnetic energy harvesters, based on Faraday's law of induction, usually consists of a coil and a moving magnet, resulting to an alternating magnetic flux. The electricity is generated by the relative movement of the magnet and coil. Generally, the amount of generated electricity depends upon the strength of the magnetic field, the velocity of the relative motion and the number of turns of the coil.

Furthermore, it has been demonstrated that nonlinear techniques, particularly those based on the Synchronized Switching techniques, can be derived in several systems and schemes, using dual transformations of the actuator or the controlled electrical quantity [28]. In fact, such energy extraction strategies have also been extended to electromagnetic vibration energy harvesters. One good example is the one developed by Arroyo *et al.*, namely the SMFE (Synchronous Magnetic Flux Extraction) technique, which provides a significant optimization of the energy transfer irrespective of the load impedance [29].

Although the majority of energy harvesters that have been so far studied and developed mainly focused on a single energy conversion mechanism, a recent trend consists in combining multiple energy conversion effects, such as piezoelectric and electromagnetic transduction, in a single device, leading to the concept of hybrid energy harvesting [30, 31, 32, 33, 34, 35, 36]. Nevertheless, most of these works mainly focused on the energy conversion mechanism, and very few actually considered the energy harvesting process on the circuit side. Table 1 gives an overview of the voltage and

Table 1: Comparison of voltage and power outputs from hybrid piezoelectric-electromagnetic energy harvesting systems (*Std.* stands for Standard circuit, *Gain PZT* and *Gain EM* stand for the energy gain with respect to the sole use of piezoelectric and electromagnetic system respectively)

Reference	V_p	V_{em}	P_p	P_{em}	P_{hyb}	Gain PZT	Gain EM
	60 V (Std.)		80 mW (Std.)			300 % (Std.)	
[31]	100 V (SSHI)	-	200 mW (SSHI)	-	250 mW	25 % (SSHI)	-
	3.5 V (0.2g)	40 mV (0.2g)	0.085 mW (0.2g)	0.14 mW (0.2g)			
[33]	9.75 V (0.45g)	150 mV (0.45g)	0.5 mW (0.45g)	1.19 mW (0.45g)	-	-	-
[35]	3 V	0.12 V	250 µW	244µW	-	-	-
[32]	8 V	0.4 V	1.65 mW	2.18 mW	2.26 mW	37 %	4 %
[30]	-	-	1.1 mW	0.96 mW	1.2 mW	10 %	30 %
[34]	0.35 V	0.012 V	40 µW	1.16 µW	-	-	-

power outputs from such hybrid systems: it is evident the high difference in the voltage outputs between the piezoelectric and the electromagnetic systems, making the latter ones not compatibles with the former ones. Moreover, the peak powers of the two systems are characterized by different values of optimal loads: extracting the energy from the hybrid system would then require an additional stage of load adaptation, hence introducing additional complexity to the circuit and power losses.

To overcome these main drawbacks when considering hybrid piezoelectric-electromagnetic energy harvesters, this paper proposes a hybrid energy harvesting electrical interface based on the coupling of these two energy conversion mechanisms. The model is derived from the previously stated SSHI interface, whose passive inductance is advantageously replaced by an electromagnetic generator, thus making active every constitutive electrical component of the interface. This produces an immediate enhancement of the final energy that can be extracted without adding significant complexity to the systems in terms of electrical components and space. A particular attention is paid to the resulting enhancement of the piezoelectric element output voltage due to the synchronized switching interface. The paper is organized as follows: section II introduces the principles and the operations of the proposed technique; section III exposes in detail the theoretical analysis giving the output energy that can be extracted with such model, either considering constant displacement magnitude or taking into account the damping effect at resonance; a preliminary theoretical discussion is illustrated in section IV; section V aims at exposing the experiments carried out in order to validate such model along with comparative discussion; Finally, section VI briefly concludes the paper.

2. Principles

The aim of this section is to recall the basic principles of energy harvesting using the standard and the SSHI technique and to introduce the main idea and motivation behind the proposed hybrid

₇₂ switching configuration.

2.1. Standard

₇₄ In the standard interface circuit, a diode rectifier bridge followed by a filtering capacitor C_s and

₇₅ a load R_L is directly connected to the piezoelectric element, as shown in Fig. 1a. This is basically

₇₆ the simplest circuit for rectifying an AC voltage, as well as the most used one for energy harvesting

₇₇ applications. The rectifier bridge is assumed to be perfect and the rectified voltage V_{DC} is assumed

₇₈ to be constant, which is a good approximation if the time constant $R_L C_s$ is much larger than the

₇₉ mechanical oscillation half-period. Fig. 1b depicts the typical voltage, displacement and current

₈₀ waveforms of such configuration:

- ₈₁ from t_1 to t_2 the rectifier bridge is blocked and the piezovoltage varies with the displacement
  ₈₂ with an off-set introduced by the previous energy harvesting process;

- ₈₃ from t_2 to t_3 the absolute piezovoltage V_p equals the rectified voltage V_{DC} so that the rectifier
  ₈₄ bridge is conducting and energy transfer occurs from the piezoelectric element to the load;

- ₈₅ after t_3, the bridge rectifier is blocked again and the piezovoltage goes back to open-circuit
  ₈₆ condition;

- ₈₇ from t_3 to t_4 the piezovoltage varies again with the displacement until the condition $|V_p| =$
  ₈₈ $-V_{DC}$ is reached so that the rectifier conducts again and a new energy transfer occurs.

2.2. Parallel SSHI

₉₀ The parallel SSHI interface consists in adding a nonlinear processing circuit in parallel with

₉₁ the piezoelectric element, as shown in Fig. 2a. This nonlinear processing circuit is composed of

₉₂ an electronic switch and an inductor L connected in series. The switch is almost always open
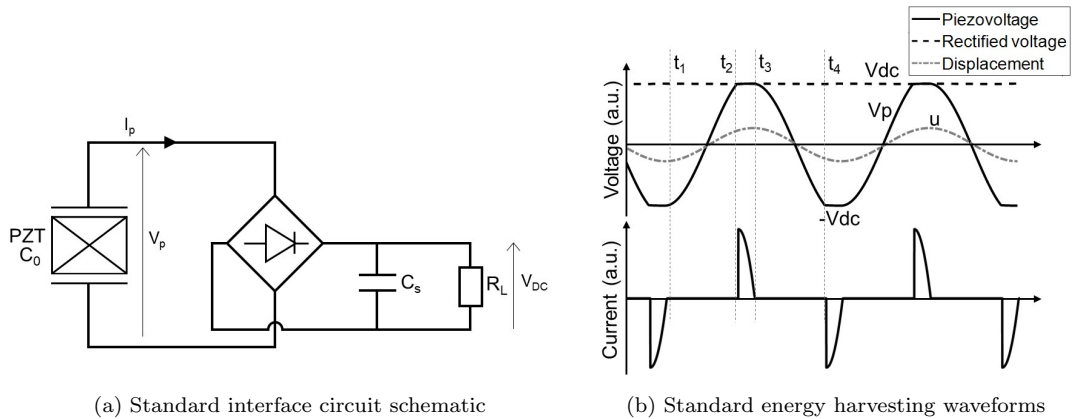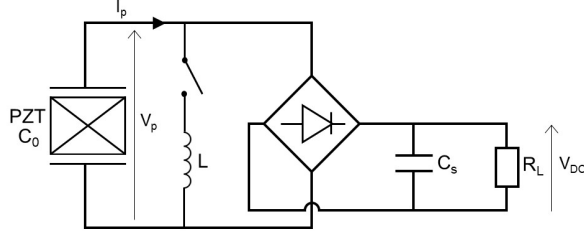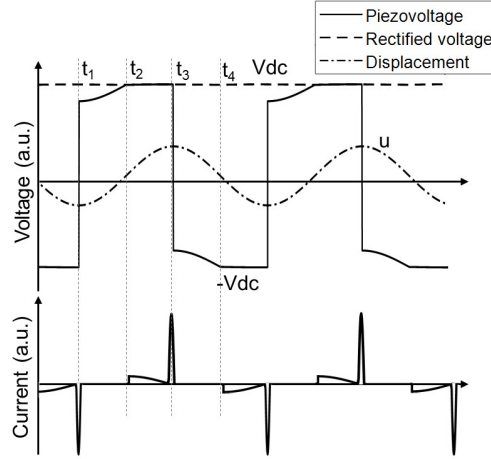

(a) Standard interface circuit schematic

(b) Standard energy harvesting waveforms

Figure 1: Standard technique

4

(a) Parallel SSHI circuit schematic

(b) SSHI waveforms

Figure 2: SSHI technique

except when an extremum in the displacement occurs. At this instant, the switch is briefly turned on, establishing an oscillating electrical network made by the inductance L and the piezoelectric clamped capacitance C_0. After half an electrical period, defined as equation (1), the switch is again turned off, resulting in a quasi-instantaneous inversion of the voltage V.

$$t_i = \pi\sqrt{LC_0} \tag{1}$$

The voltage inversion is however not perfect (due to the losses in the switching branch) and characterized by the inversion coefficient defined as:

$$\gamma_0 = e^{-\frac{\pi}{2Q_i}} \tag{2}$$

where Q_i is the electrical quality factor of the LC_0 circuit. Fig. 2b depicts the typical voltage, displacement and current waveforms of the SSHI configuration:

- from t_1 to t_2 the rectifier bridge is blocked and the piezovoltage varies with the displacement with an off-set introduced by the previous voltage inversion;

5

- from t_2 to t_3 the absolute piezovoltage V_p equals the rectified voltage V_{DC} so that the rectifier bridge is conducting and energy transfer occurs from the piezoelectric element to the load;

- at t_3, which corresponds to a displacement extremum, the switch is turned on (explaining the current spikes) and the piezoelectric voltage is reversed. Its absolute value remains lower than the rectified voltage V_{DC} so the rectifier bridge is blocking again;

- from t_3 to t_4 the piezovoltage varies again with the displacement until the condition $|V_p| = -V_{DC}$ is reached so that the rectifier conducts again and a new energy transfer occurs.

2.3. Hybrid model

Considering the SSHI interface, one can note that the inductor can play an active role if coupled with a permanent magnet that is moving relatively to it. In fact, the idea behind the proposed hybrid model is to convert the inductor from a passive electrical component to an active electromagnetic system leading to the concept of hybrid energy harvesting. Thus, the combination of the two energy conversion effects on the same harvesting system induces an enhancement of the output voltage of the piezoelectric element, as depicted in Fig. 3, resulting in a higher harvested energy without significant loss in terms of space. The general resulting circuit is illustrated in Fig. 4 and its operations will be explained in detail in the following sections. The reason behind the employment of the two transducers in such configuration, rather than extracting the energy from them separately, lies in the in the duality of the nature of the two transducer systems: the piezoelectric can be electrically modelled as a current source in parallel with a capacitance, whereas an electromagnetic system can be modelled as a voltage source in series with an inductance [37]. The former is characterized by high levels of voltage and low current while the latter is distinguished by high levels of current and low voltage, so interfacing each of the two systems to a single harvesting stage would lead to a more complex electrical interface (for instance, by employing DC/DC converters), seeing the big difference on the voltage/current outputs, and adding complexity to the circuit always translates into energy losses. On the other hand, the proposed SSH-EM (Synchronized Switch Harvesting on ElectroMagnetic system) switching technique is not sensitive to the

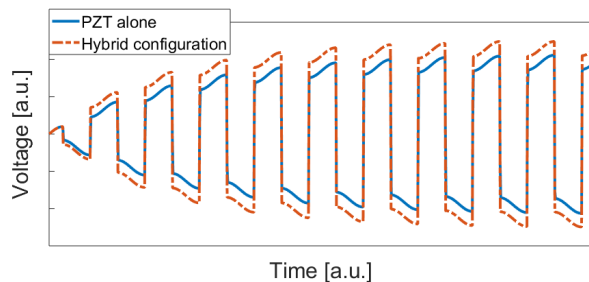Figure 3: Voltage waveforms of the switching on electromagnetic system strategy and comparison with SSHI technique

(a) Default configuration
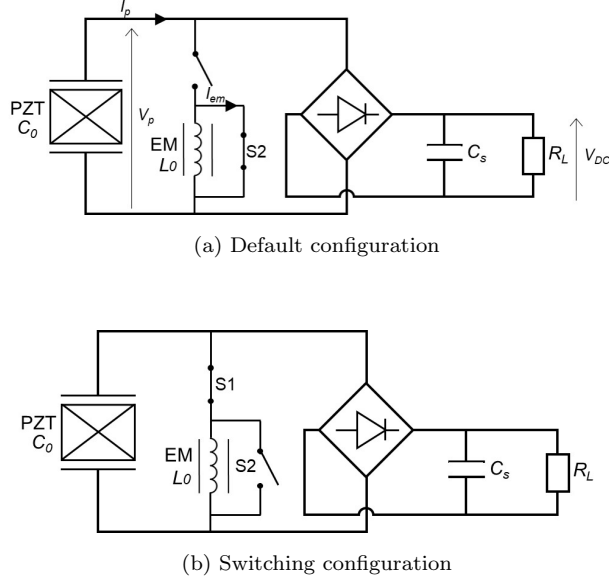

(b) Switching configuration

Figure 4: Hybrid model circuit schematic

129 difference in the voltage and current outputs that exists between the two transducers, as they are
130 made to interact as a LC oscillator, resulting in the magnification of the voltage seen in Fig. 3.

3. Theoretical development

132 In the previous section, the basic principles of the proposed model have been introduced. Con-
133 sequently, it is now possible to set up the theoretical development allowing the prediction of the
134 extracted energy and output power of such scheme.

135 Assuming linear elasticity, vibrating mechanical structures excited near one resonance frequency
136 can be modeled by a second-order mass-spring-damper system [38]. The schematic of such inertial
137 generators can be applied both to piezoelectric and electromagnetic generators [39], as shown in
138 Fig. 5, where M is the equivalent dynamic mass bonded on a spring K (modeling the stiffness of
139 the mechanical structure) and a damper C (modeling the mechanical losses).

140 As previously stated, from an electrical point of view, a piezoelectric generator is equivalent
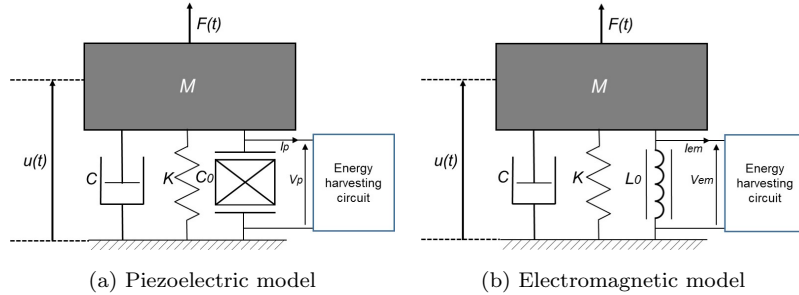

(a) Piezoelectric model

(b) Electromagnetic model

Figure 5: Equivalent mechanical models of piezoelectric and electromagnetic generators

7

to a current source proportional to the relative vibration velocity $\dot{u}$ connected in parallel with a capacitor while an ideal electromagnetic generator can be modelled as a velocity dependent voltage source in series with an inductor [28]. Neglecting the transducers' electrical losses (especially in the electromagnetic case), the constitutive electromechanical equations of such model are therefore given by:

$$\begin{cases} M\ddot{u} + C\dot{u} + K^{E,H}u = F - \alpha V_p - \beta I_m \\ I_p = \alpha\dot{u} - C_0\dot{V}_p \\ V_{em} = \beta\dot{u} - L_0\dot{I}_{em} \end{cases} \tag{3}$$

where u is the displacement of the structure (assumed to be sinusoidal in the followings), V_p and V_{em} the piezoelectric and electromagnetic voltages respectively and I_p and I_{em} the piezoelectric and electromagnetic currents respectively; α and β are the force factors of the piezoelectric and electromagnetic elements respectively; Finally, C_0 represents the piezoelectric clamped capacitance and L_0 the inductance of the electromagnetic transducer at rest.

3.1. Switching process

Fig. 6 gives a rough schematic of the proposed hybrid model without the consideration of the rectifying circuit. This scheme can be divided into two sub-sections, one corresponding to the piezoelectric (PZT) insert and the other one corresponding to the electromagnetic (EM) element. Most of the time, the piezoelectric transducer is left in open circuit conditions while the electromagnetic system is short-circuited, as depicted in Fig. 6a. Under these conditions, the piezoelectric voltage and the electromagnetic current vary proportionally to the mechanical displacement, following equation (4) and (5):

$$I_p = 0 \Rightarrow \dot{V}_p = \frac{\alpha}{C_0}\dot{u} \tag{4}$$

$$V_{em} = 0 \Rightarrow \dot{I}_{em} = \frac{\beta}{L_0}\dot{u} \tag{5}$$

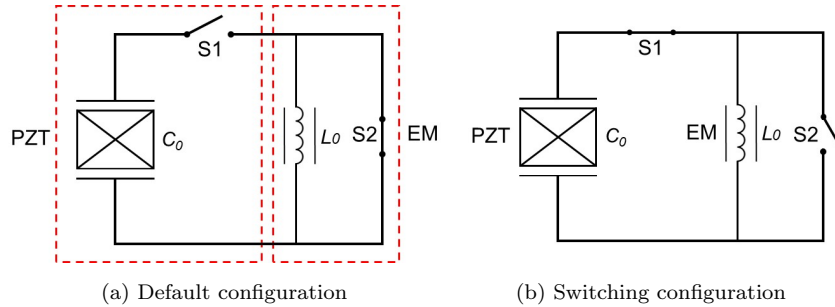

(a) Default configuration   (b) Switching configuration

Figure 6: Circuit schematic

8

When the mechanical displacement reaches a maximum or a minimum value (i.e. when the mechanical speed cancels), the electronic switches S1 and S2 are briefly turned on and off respectively, as shown in Fig. 7, so that the piezoelectric and the electromagnetic generators are electrically connected, establishing an oscillating electrical $L_0 - C_0$ circuit composed by the electromagnetic inductance L_0 and the piezoelectric clamped capacitance C_0. As a result, a current flow appears as:

$$L_0 \ddot{q} + r_s \dot{q} + \frac{q}{C_0} = 0 \tag{6}$$

where r_s represents the equivalent linear losses due to switching interface and q is the electric charge of the piezoelectric element. Differently from standard synchronized switching interfaces, having null initial current flow, Eq. (6) is solved considering non-zero initial current condition, as an effect of the addition of the electromagnetic generator, and considering the voltage across the piezoelectric element:

$$\begin{cases} q_0 = C_0 V_p = \alpha u_M \\ \dot{q}_0 = I_{em} = \frac{\beta}{L_0} u_M \end{cases} \tag{7}$$

hence, the voltage and the current oscillation are defined as:

$$V(t) = e^{-\frac{r_s}{2L_0 \omega_{sw}} t} \left[V_M \cos(\omega_{sw} t) + \frac{I_M}{C_0 \omega_{sw}} \sin(\omega_{sw} t) \right] \tag{8}$$
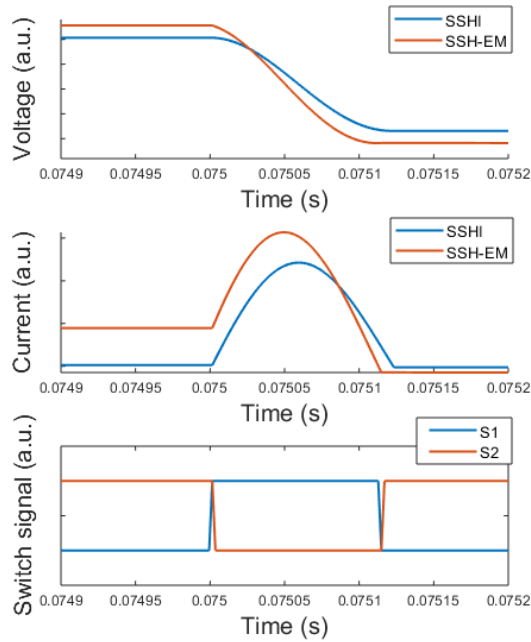

Figure 7: Voltage and current waveforms and switching signals

$$I(t) = e^{-\frac{r_s}{2L_0\omega_{sw}}t}\big[-C_0V_M\omega_{sw}\sin(\omega_{sw}t) + I_M\cos(\omega_{sw}t)\big] \tag{9}$$

where I_M is the current provided by the electromagnetic element (I_{em}) at the switching instant, V_M corresponds to the maximum output voltage provided by the piezoelectric component (V_p) at the same switching instant and ω_{sw} refers to the resonance frequency of the L_0C_0 oscillator (*i.e.* $1/\sqrt{L_0C_0}$). In order to achieve voltage inversion, the switch S1 must be again turned off (and S2 turned back on) when the current is null. Therefore, as a consequence of the contribution of the electromagnetic generator (which has lead to non-zero initial current condition), the equivalent inversion coefficient for the hybrid harvester model is given by:

$$\gamma_P = e^{-\frac{r_s\pi}{2L_0\omega_{sw}}} e^{-\frac{r_s}{2L_0\omega_{sw}}\arctan(\frac{I_M}{C_0V_M\omega_{sw}})} \sqrt{1 + \left(\frac{I_M}{C_0V_M\omega_{sw}}\right)^2} \tag{10}$$

noting that the parameter $\gamma_0 = e^{-\frac{r_s\pi}{2L_0\omega_{sw}}}$ corresponds to the inversion coefficient of the non-hybrid synchronized switching case, as defined by equation (2).

Consequently, considering the steady-state case, the relation between the output voltage magnitudes before (V_M) and after (V_m) the inversion process are finally given by:

$$\begin{cases} V_M - V_m = 2\frac{\alpha}{C_0}u_M \\ V_m = \gamma_P V_M \end{cases} \tag{11}$$

Typical waveforms of the switching event are depicted Fig. 7, giving a comparison with respect to the classical SSHI technique. It is interesting to point out the improvement in the voltage inversion and magnification as a consequence of the contribution of the electromagnetic system that provides initial current.

3.2. Derivation of the output power

In order to give an estimation of the harvested power, constant displacement magnitude of the structure is firstly considered. This leads to not considering electromechanical damping effect in terms of mechanical vibrations, which is a good approximation for low coupled, highly damped systems, or structures excited out of their resonance frequencies. Secondly, the performance of the SSH-EM interface will be quantified taking into account this damping effect induced by the energy harvesting process (which is the case of highly coupled microgenerators excited by a constant acceleration very close to one of their resonance frequencies).

3.2.1. Constant displacement magnitude

if the structure is supposed to be driven with a constant displacement magnitude, only the second and the third constitutive equations of Eq. (3) are actually necessary in order to evaluate the extracted energy of the proposed scheme. The harvested energy (W_h) for one extraction event (between the time instants t_1 and t_2 in Fig. 8 can therefore be expressed starting from the
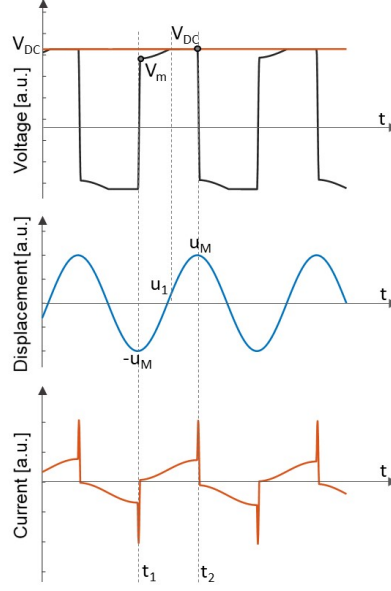
Figure 8: Voltage, displacement and current waveforms in the steady-state case

piezoelectric electrical equation of Eq. (3) and leading to the following integral function of the rectified piezoelectric voltage and current:

$$W_h = \int_{t_1}^{t_2} V_{DC} I_P \, dt = \alpha V_{DC} \int_{u_1}^{u_M} du = \alpha V_{DC}(u_M - u_1) \tag{12}$$

where u_1 and u_M refers to the displacement values when the harvesting process starts and the displacement magnitude, respectively, as shown in Fig. 8, and V_{DC} the value of the rectified voltage, assumed to be constant.

Considering an energy scavenging process on a positive (resp. negative) voltage, the harvesting process stops when the current cancels — which occurs on minimum (resp. maximum) displacements. Hence, after energy transfer and inversion process, the system is left open-circuit. Moreover, in the DC case, $V_M = V_{DC}$ so that $V_m = \gamma_P V_{DC}$. Consequently, as shown by Eq. (13), the equivalent inversion coefficient in that case actually depends on the rectified voltage V_{DC}, so that it will be noted as $\gamma_P(V_{DC})$ in the followings.

$$\gamma_P(V_{DC}) = \gamma_0 e^{-\frac{r_s}{2L_0 \omega_{sw}} \arctan(\frac{I_M}{C_0 V_{DC} \omega_{sw}})} \sqrt{1 + \left(\frac{I_M}{C_0 V_{DC} \omega_{sw}}\right)^2} V_{DC} \tag{13}$$

Consequently, integrating the second equation equation of Eq. (3) yields the expression of the voltage as follows (considering the evolution from $\gamma_P(V_{DC})V_{DC}$ to V_{DC}):

$$\begin{cases} V = \frac{\alpha}{C_0} u + A \\ \gamma_P(V_{DC}) \cdot V_{DC} = -\frac{\alpha}{C_0} u_M + A \end{cases} \tag{14}$$

where A is an integration constant.

11

The value of the displacement u_1 when the harvesting process starts can be obtained by considering the voltage equals to V_{DC}, as provided by the following expressions:

$$V_{DC} = \frac{\alpha}{C_0}(u_1 + u_M) + \gamma_P(V_{DC}) \cdot V_{DC} \tag{15}$$

$$V_{DC}(1 - \gamma_P(V_{DC})) = \frac{\alpha}{C_0}(u_1 + u_M) \tag{16}$$

hence, yielding:

$$u_1 = \frac{C_0}{\alpha}V_{DC}(1 - \gamma_P(V_{DC})) - u_M \tag{17}$$

Combining Eq. (17) and Eq. (12), gives:

$$W_h = V_{DC}[2\alpha u_M + C_0(V_{DC} - \gamma_P(V_{DC}) \cdot V_{DC})] \tag{18}$$

As two energy harvesting processes occur per period, the expression of the output power can be obtained as a function of the electromechanical parameters as:

$$P = 2f_0 W_h = 2f_0 V_{DC}[2\alpha u_M + C_0 V_{DC}(1 - \gamma_P(V_{DC}))] \tag{19}$$

where f_0 denotes the mechanical vibration frequency. Additionally, the harvested power can also be expressed as a function of the squared value of the voltage V_{DC} and the resistance R_L, giving:

$$P = \frac{V_{DC}{}^2}{R_L} \tag{20}$$

In order to make the analysis independent from the system parameters, the output voltage can be normalized with respect to the open-circuit voltage amplitude and the resistance with respect to the optimal resistance of the piezoelectric element in the standard case, as illustrated below:

$$\begin{cases} \tilde{V} = \frac{V_{DC}}{V_{oc}} = \frac{V_{DC}}{\frac{\alpha}{C_0}u_M} \\ \tilde{R} = \frac{R_L}{R_{opt_{st}}} = \frac{R_L}{1/4 f_0 C_0} \end{cases} \tag{21}$$

Additionally, substituting the value for I_M following Eq. (5), introducing the ratio r between the terms $\frac{\beta^2}{L_0}$ and $\frac{\alpha^2}{C_0}$, and substituting Eq. (13) into Eq. (18), we finally obtain the following non-dimensional 3rd order polynomial expression:

$$2\tilde{V}^3\left(2 + \tilde{R}(1 - \gamma_0)\right) - 2\tilde{V}^2\tilde{R}\left(2 + \gamma_0 \frac{1}{2Q_i}\sqrt{r}\right) - \tilde{V}\tilde{R}\gamma_0 r + \tilde{R}\gamma_0 r^{3/2}\frac{1}{2Q_i} = 0 \tag{22}$$

of which approximated solution is given by:

$$\tilde{V} = \frac{2\tilde{R}\left(2 + \gamma_0 \frac{1}{2Q_i}\sqrt{r}\right)}{6\left(2 + \tilde{R}(1 - \gamma_0)\right)}\left(1 + 2\sqrt[3]{1 + \frac{18\left(2 + \tilde{R}(1 - \gamma_0)\right)\tilde{R}\gamma_0 r}{8\tilde{R}^2\left(2 + \gamma_0 \frac{1}{2Q_i}\sqrt{r}\right)}}\right) \tag{23}$$

12

₂₂₈ where the expressions used to calculate the voltage expressed in Eq. (23) are detailed in Appendix

₂₂₉ A.

₂₃₀ Consequently, it is possible to express the harvested power combining equations (23), (19) and (20)

₂₃₁ and considering the dimensional parameters, yielding:

$$P = \frac{\tilde{V}^2}{\tilde{R}} \frac{4\alpha^2}{C_0} f_0 u_M \tag{24}$$

₂₃₂ *3.2.2. Constant driving force magnitude*

₂₃₃ the operation of converting mechanical energy into electrical energy from a coupled system using

₂₃₄ piezoelectric and electromagnetic mechanisms will cause multiple induced damping effects, thus

₂₃₅ causing a reduction of the available effective mechanical energy in terms of relative displacement

₂₃₆ u and relative velocity $\dot{u}$, thereby reducing the induced piezoelectric voltage (directly proportional

₂₃₇ to the displacement) and the induced electromotive force (directly proportional to the velocity),

₂₃₈ respectively; hence, the total harvested power of the coupled system is reduced in return. For sake

₂₃₉ of simplicity, from now onwards the analysis will be conducted considering an equivalent value of

₂₄₀ the inversion factor γ_P, which takes into account the rectified voltage calculated in the previous

₂₄₁ section (written as $\gamma_P(V_{DC})$).

₂₄₂ In this case, the energy balance of the structure is considered. Multiplying both terms of the first

₂₄₃ constitutive equation of Eq. (3) by the velocity and integrating over half a period leads to:

$$M \int_{t_1}^{t_2} \ddot{u}\dot{u}\,\mathrm{d}t. + C \int_{t_1}^{t_2} \dot{u}\dot{u}\,\mathrm{d}t. + K^{E,H} \int_{t_1}^{t_2} u\dot{u}\,\mathrm{d}t. = \int_{t1}^{t2} \dot{u}\,\mathrm{d}u. - \alpha \int_{t_1}^{t_2} V_p\dot{u}\,\mathrm{d}t. - \beta \int_{t_1}^{t_2} I_{em}\dot{u}\,\mathrm{d}t. \tag{25}$$

₂₄₄ Particularly, in steady state, it is possible to the define the transferred energy of the piezoelectric

₂₄₅ element as the sum of electrostatic energy stored on the piezoelectric clamped capacitance and the

₂₄₆ energy absorbed by the connected load:

$$\alpha \int_{t_1}^{t_2} V_p\dot{u}\,\mathrm{d}t. = \frac{1}{2}C_0[V_{DC}{}^2 - (\gamma_P(V_{DC}) \cdot V_{DC})^2] + \frac{V_{DC}{}^2}{R_L}\frac{T}{2} = \frac{1}{2}C_0 V_{DC}{}^2[1 - (\gamma_P(V_{DC}))^2] + \frac{V_{DC}{}^2}{R_L}\frac{T}{2} \tag{26}$$

₂₄₇ where $\gamma_P(V_{DC})(V_{DC})$ stands for the implicit inversion coefficient in the DC case.

₂₄₈ As per the mechanical energy converted into electrical energy by the electromagnetic system, the

₂₄₉ energy transfer occurs when the electromagnetic system is short-cicruited:

$$\beta \int_{t_1}^{t_2} I_{em}\dot{u}\,\mathrm{d}t. = \frac{1}{2}L_0(2I_{sc})^2 \tag{27}$$

₂₅₀ When considering steady state conditions, there is no variation of the potential elastic energy

₂₅₁ between instant t_1 and t_2 as well as a null kinetic energy at those instants for a system excited at

₂₅₂ resonance, thus yielding:

$$\frac{\pi}{2}F_M u_M = \frac{\pi}{2}C u_M{}^2\omega + \frac{1}{2}C_0 V_{DC}{}^2[1-(\gamma_P(V_{DC}))^2] + \frac{V_{DC}{}^2}{R_L}\frac{T}{2} + \frac{1}{2}L_0(2I_{sc})^2 \tag{28}$$

where F_M stands for the driving force magnitude.

Using Eq. (26) and the second constitutive equation of Eq. (3), the recified voltage can be expressed according to Eq. (29), while Eq. (30) recalls the electromagnetic current under short-circuit conditions:

$$V_{DC} = \frac{2R_L\alpha}{RC_0(1-\gamma_P(V_{DC}))\omega+\pi}\omega u_M \tag{29}$$

$$I_{sc} = \frac{\beta^2}{L_0}u_M \tag{30}$$

Hence, the expression of the displacement magnitude at resonance frequency when taking into account the damping effect leads to:

$$u_m = \frac{F_m}{C\omega + \dfrac{4R_L\omega\alpha^2}{\pi}\dfrac{\left(R_L C_0(1-\gamma_P(V_{DC}))\omega+2\pi\right)}{\left(R_L C_0(1-\gamma_P(V_{DC}))\omega+\pi\right)^2} + \dfrac{4}{\pi}\dfrac{\beta^2}{L_0}} \tag{31}$$

and the associated harvested power is thus given by:

$$P = \frac{V_{DC}{}^2}{R_L} = \frac{4R_L\alpha^2}{\left(R_L C_0(1-\gamma_P(V_{DC}))\omega+\pi\right)^2}\omega^2 u_M{}^2 \tag{32}$$

Recalling the expression of the displacement and the power from the SSHI case as per Eq. (33) and (34) respectively [23], the SSH-EM and SSHI systems are in this way easy to correlate (SSHI being a particular case of SSH-EM with $\beta = 0$ and $\gamma_P = \gamma_0$), thus conveniently allowing a comparison between the two techniques, as it will be discussed in the next section.

$$u_{M_{SSHI}} = \frac{F_m}{C\omega + \dfrac{4R_L\omega\alpha^2}{\pi}\dfrac{\left(R_L C_0(1-\gamma_0)\omega+2\pi\right)}{\left(R_L C_0(1-\gamma_0)\omega+\pi\right)^2}} \tag{33}$$

$$P_{SSHI} = \frac{V_{DC}{}^2}{R_L} = \frac{4R_L\alpha^2}{\left(R_L C_0(1-\gamma_0)\omega+\pi\right)^2}\omega^2 u_{M_{SSHI}}{}^2 \tag{34}$$

4. Theoretical discussion

Based on the modelling developed in the previous sections, it is proposed here to investigate the performance of the SSH-EM configuration, and compare it with the original SSHI and standard interfaces. The performance is first evaluated considering the structure driven with a constant displacement amplitude and then considering a constant force amplitude. It must be noted, however, that the power losses and the electromagnetic current phase shift due to the coil resistance of the

electromagnetic system are not taken into account.

As a first theoretical comparison, Fig. 9 evaluates the relation between the ratio r of the parameters $\frac{\beta^2}{L_0}$ and $\frac{\alpha^2}{C_0}$ and the improvement of the inversion coefficient γ_P. This figure demonstrates how incrementing the contribution of the electromagnetic element, in terms of possible transferred energy, can lead to higher values of inversion coefficient, thus inducing voltage enhancements. As a restult, an increase of the output voltage translates to an increase of the harvested power, as shown in Fig. 10. The figure plots the evolution of the power generated from the hybrid system, following to Eq. (25), as a function of the load and the same ratio r coefficient, for different values of the original SSHI inversion coefficient (*i.e.*, γ_0).

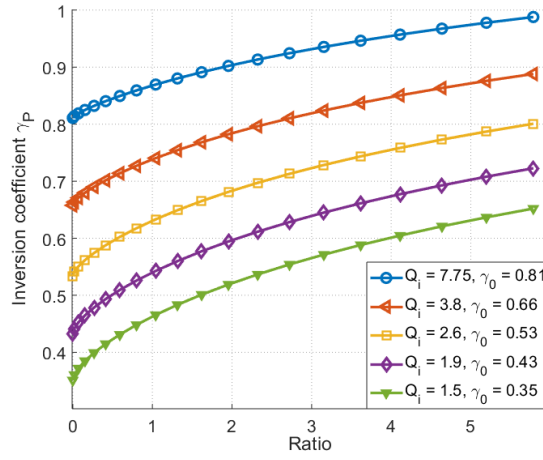In order to conduct the theoretical evaluation as independently as possible from the system

Figure 9: Inversion coefficient γ_P as a function of the ratio for several values of electrical quality factor Q_i
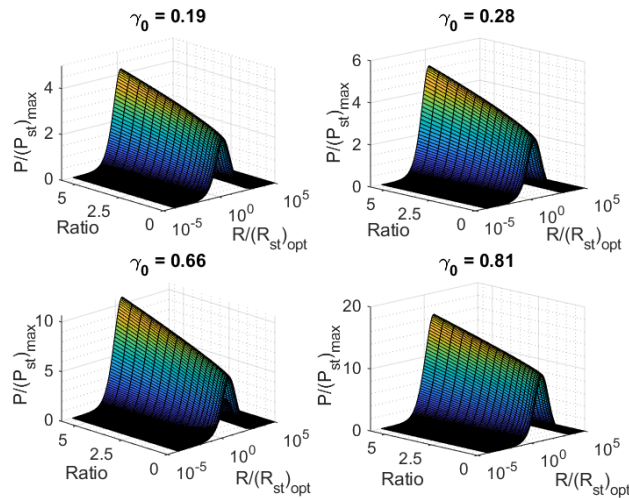

Figure 10: Normalized harvested power (w.r.t. maximal harvested power in the standard approach) as a function of the ratio and the normalized load (w.r.t. the optimal load in the standard approach) for several initial inversion factors

15

parameters, the harvested power has been normalized with respect to the maximum power in the standard case, and the resistance with respect to the optimal resistance in the standard case, as defined in Eq. (35),(36) [20]:

$$(P_{st})_{max} = \frac{\alpha^2}{C_0} f_0 u_M{}^2 \tag{35}$$

$$(R_{st})_{opt} = \frac{1}{4 f_0 C_0} \tag{36}$$

The chart in Fig. 10 demonstrates that, as the ratio increases (*i.e.*, as the contribution of the electromagnetic system becomes more relevant), the resulting electrical power increases as well in a quite similar way (relatively speaking), whatever the initial SSHI inversion coefficient. It can be noted that for $r = 0$, therefore for $\beta^2/L_0 = 0$, the technique is strictly equivalent to the SSHI technique.

In order to better evaluate the power gain that can be achieved with respect to the SSHI scheme, Fig. 11 depicts the evolution of this gain as a function of the same ratio term (adopted in the previous graphs) for different values of the electrical quality factor Q_i. It is interesting to note how the power gain reaches on optimal value when considering an electrical quality factor Q_i equal to 1.9 (*i.e.* $\gamma_0 = 0.43$).

Moreover, the comparison of the SSH-EM approach with the SSHI technique and the sole use of electromagnetic and piezoelectric elements is shown in Fig. 12. The analysis has been conducted considering two different electrical quality factors (which corresponds to two different initial SSHI inversion coefficients) and two values of ratio r (by making varying the electromagnetic force factor β). In this example, the electromagnetic and piezoelectric powers (curves 4-5-6 of Fig. 12) have been evaluated considering a simplified linear circuit (*i.e.* without considering the rectification stage). As a matter of fact, the main issue when using a full bridge rectifier for
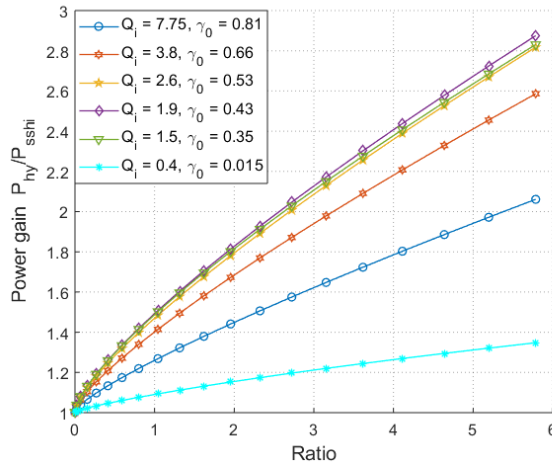

Figure 11: Extracted power gain compared to SSHI interface for several values of electrical quality factor Q_i
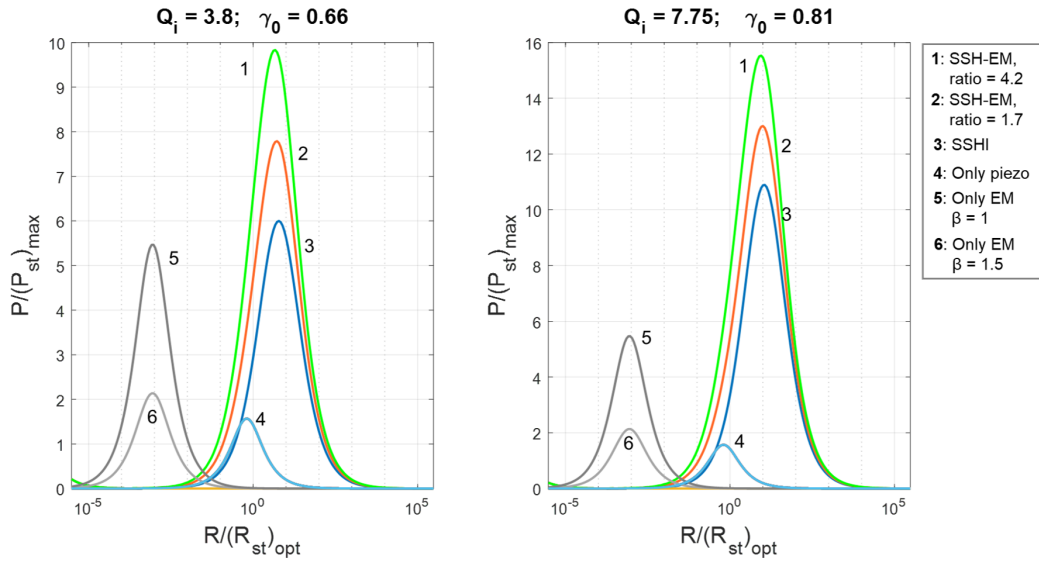
16

Figure 12: Normalized harvested power (w.r.t. maximal harvested power in the standard approach) as a function of the normalized load (w.r.t. the optimal load in the standard approach) for different techniques, electrical quality factor and ratios

electromagnetic energy harvesting systems is that a large amount of energy can be lost in the diodes if the open-circuit voltage amplitude is lower the diode threshold voltage (which is typical for many electromagnetic systems - and for the one in this case)[1]. Nevertheless, it is evident how the SSH-EM technique allows achieving power output much greater even when considering the ideal case of the sum of the single piezoelectric and electromagnetic powers, considering that for the latter an additional load adaptation stage is required (therefore introducing additional losses and lowering the hybrid power levels). This confirms the advantage of employing the two transducers for energy harvesting purposes using the proposed SSH-EM approach.

When taking into account the damping effect, two important figures of merit are normally used to compare different electromechanical systems: the mechanical quality factor Q_m and the squared coupling coefficient of the structure k_p^2, the former representing the available amount of energy while the latter reflecting the available energy that can actually be converted and directly related to the amount of active material. Fig. 13 thus relates the theoretical maximum powers using the SSH-EM, SSHI and the linear resistive technique in function of the FoM $k_p^2 Q_m$. Additionally, the case of the sole use of electromagnetic transducer has been taken into consideration, plotting its theoretical maximum power in function of the FoM $k_{em}^2 Q_m$. For each technique, the power has

---

[1]It must be noted that a comparison between the output powers that can be achieved with the proposed SSH-EM technique and a combination of nonlinear harvesting for both piezoelectric and electromagnetic transducers (for instance, by employing simultaneously the SSHI and the SMFE technique) has not been considered and it would not be fair, as the latter would require two more additional electrical components (an inductance – for the SSHI – and a capacitor – for the SMFE).
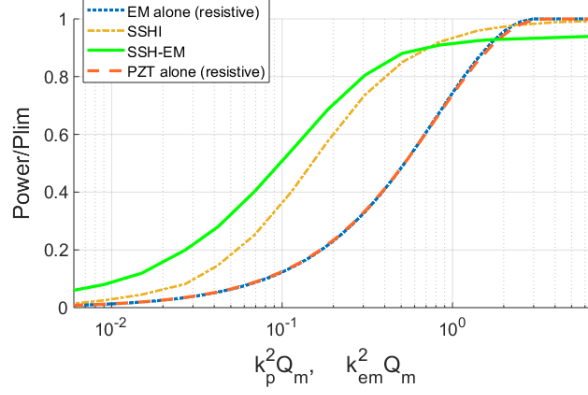
Figure 13: Normalized maximum harvested power (w.r.t. the power limit) for different techniques versus the figure of merit $k_p{}^2Q_m$ and $k_{em}{}^2Q_m$ when taking into account the damping effect

been normalized according to the power limit that can be reached, depending on the mechanical losses of the structure [23]:

$$P_{lim} = \frac{F_m{}^2}{8C} \tag{37}$$

Based on the trends of Fig. 13, the SSH-EM technique appears to be of particular interest when considering weakly coupled/highly damped structures, as the damping effect due to the combination of two energy harvesting transducers becomes more relevant in the case of high values of the figure of merit $k_p{}^2Q_m$. This is also confirmed by Fig. 14, plotting the power as a function of the figure of merit $k_{em}{}^2Q_m$, where $k_{em}{}^2$ represents the electromagnetic coupling coefficient, for different values of $k_p{}^2Q_m$. The figure clarifies how higher power gains can be achieved for low coupled/highly damped structures, as well as the existence of an optimum value of the electromag-
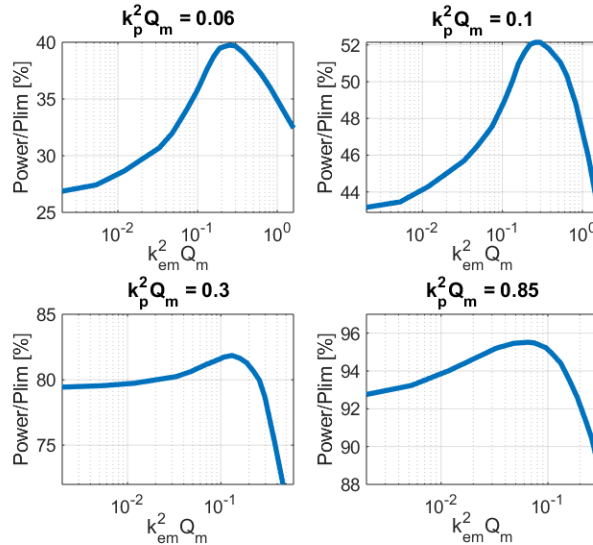

Figure 14: Normalized maximum harvested power (w.r.t. the power limit) as a function of the figure of merit $k_{em}{}^2Q_m$ for different values of $k_p{}^2Q_m$

netic coupling. Furthermore, as the piezoelectric coupling coefficient increases, this optimal value of electromagnetic coupling decreases.

5. Experimental validations

The previous discussions theoretically pointed out the advantages of employing the SSH-EM technique over previously developed nonlinear techniques, particularly when considering low coupled/highly damped structures. Hence, this section proposes to experimentally validate these theoretical predictions previously discussed.

5.1. Experimental set-up

Fig. 15a illustrates the schematic of the experimental set-up used in this study. The piezoelectric generator is composed of a piezoelectric buzzer with an additional permanent magnet (NdFeB) mounted on it. The permanent magnet allows the coupling of the electromagnetic generator to the piezoelectric one by placing a coil along the axis of motion of the magnet, as shown in Fig. 15b. The permanent magnet shown in the figure is mounted in this particular way after optimizing
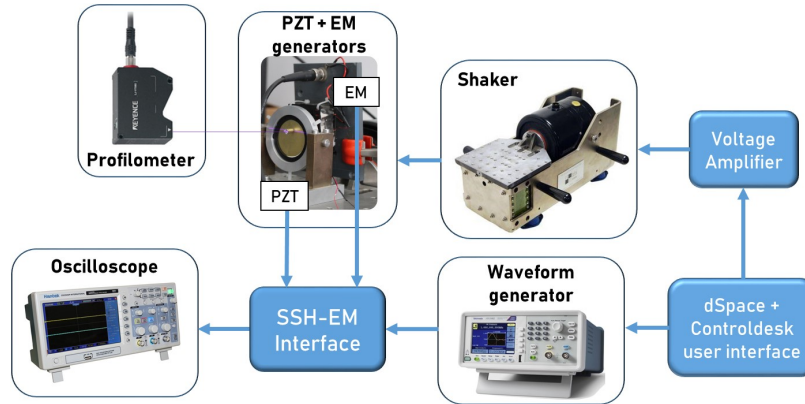
(a) Experimental set-up schematic
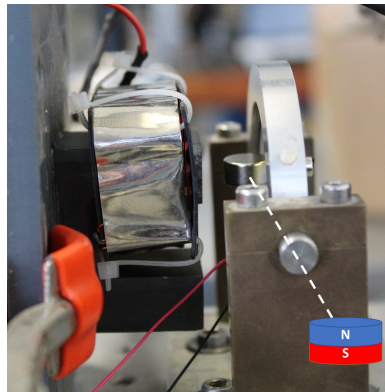
(b) EM and PZT transducers

Figure 15: Experimental set-up

19

different orientations of it. Mounting the magnet with the north/south pole completely attached to the piezoelectric buzzer, would lead to higher clamping of the piezoelectric transducer, thus leading to less variation of its displacement. Hence, to avoid this effect, the magnet is oriented as shown in Fig. 15b, which gives the optimal output. Although the magnet has axial magnetization, the closing through the bottom and the top ferrite legs still allows significant flux variation through the coil. The ferrite also permits a much higher inductance as compared to the case of generators without the core, yielding higher reactance than the resistive part of the coil. Moreover, a 0.25mm-thick nickel–iron soft ferromagnetic alloy with very high permeability, is wrapped around the coil as a shield against static or low-frequency magnetic fields from the surroundings (the shaker, for instance). The global system is mounted on a shaker driven by a controlled dSpace card (RTI 1104) which generates a sinusoidal acceleration with an amplitude of 3.8 ms^{-2} (0.39g) with the help of a voltage amplifier. The dSpace card is also used to trigger a waveform generator controlling the switching circuit, at extremum displacements. A laser displacement sensor (Keyence LJ-V7000) is used to monitor the displacement of the permanent magnet as well as an oscilloscope for monitoring the voltage and current waveforms. Finally, a digital multimeter is used to measure the DC voltage on the load R_L connected to the SSH-EM interface along with a smoothing capacitor and a rectifier bridge.

5.2. Model parameters identification

Preliminary experimental measurements have been carried out in order to determine the model parameters, listed in Table 2. The parameter identification have been obtained by measuring the open circuit output voltage V_{OC}, the displacement magnitude u_M and piezoelectric clamped capacitance C_0, thus obtaining the value of the piezoelectric force factor α defined as $C_0 \times (V_{OC}/u_M)$. The same procedure was followed for the identification of the parameters for the electromagnetic generator, this time measuring the output short-circuit current I_{SC}, the displacement magnitude u_M and the coil inductance L_0, thus obtaining the value of the electromagnetic force factor β defined as $L_0 \times (I_{SC}/u_M)$. C_0 and the coil parameters (inductance and resistance) have been obtained by the use of a LCR meter. The inversion factor γ_P has been measured from the ratio between the absolute voltages after and before the inversion process. The electromechanical coupling of the piezoelectric system $k_p{}^2$ is derived from the short-circuit and the open-circuit piezoelectric resonance frequencies, when the electromagnetic element is open-circuited. On the contrary, the electromechanical coupling of the electromagnetic element $k_{em}{}^2$ is derived from the short-circuit and the open-circuit electromagnetic resonance frequencies, when the piezoelectric element is short-circuited. Consequently, it is possible to derive 4 different values of stiffness for the studied system based on the open-circuit and short-circuit configuration of the two transducers:

$$K_{DH} = \frac{\alpha^2}{C_0} \frac{f_{DH}{}^2}{f_{DH}{}^2 - f_{EH}{}^2} = \frac{\alpha^2}{C_0} \frac{1}{k_p{}^2} \tag{38}$$

20

Table 2: Model parameters (PZT and EM respectively refer to piezoelectric and electromagnetic transducers; "oc" and "sc" respectively stand for "open-circuit" and "short-circuit")

PZT clamped capacitance, C_0	67.85 nF
EM coil inductance, L_0	28.17 mH
EM coil resistance, r_L	5.8 Ω
PZT force factor, α	0.0036 NV^{-1}
EM force factor, β	1.2 NA^{-1}
Mechanical quality factor, Q_m	30
Resonance frequency, PZT sc, EM oc f_{EH}	152.15 Hz
Resonance frequency, PZT oc, EM oc f_{DH}	155.33 Hz
Resonance frequency, PZT sc EM sc f_{EB}	152.63 Hz
PZT coupling coefficient, $k_p{}^2$	0.0402
EM cupling coefficient, $k_{em}{}^2$	0.0063
Stiffness (PZT sc, EM oc), K_{EH}	4.52x10^3 Nm^{-1}
Stiffness (PZT oc, EM oc), K_{DH}	4.72x10^3 Nm^{-1}
Stiffness (PZT sc, EM sc), K_{EB}	8.11x10^3 Nm^{-1}
Stiffness (PZT oc, EM sc), K_{DB}	8.06x10^3 Nm^{-1}
Dynamic mass, M	5g
Damping coefficient, C	0.335 N$m^{-1}s^{-1}$

$$K_{EH} = K_{DH} - \frac{\alpha^2}{C_0} \tag{39}$$

$$K_{EB} = \frac{\beta^2}{L_0} \frac{f_{EH}{}^2}{f_{EB}{}^2 - f_{EH}{}^2} = \frac{\beta^2}{L_0} \frac{1}{k_{em}{}^2} \tag{40}$$

$$K_{DB} = K_{EB} - \frac{\beta^2}{L_0} \tag{41}$$

where the subscripts DH and EH represent the case in which the piezoelectric element is open-circuited and short-circuited respectively, while having the electromagnetic element open-circuited, and the subscripts EB and DB represent the case in which the electromagnetic element is short-circuited while having the piezoelectric element short-circuited and open-circuited, respectively. Finally, the dynamic mass and the damping coefficient of the system are derived as:

21

$$M = \frac{K_{EH}}{\omega_{EH}^2} \tag{42}$$

$$C = \frac{M\omega_{DH}}{Q_m} \tag{43}$$

with Q_m being defined as the mechanical quality factor with respect to the -3dB bandwidth.

5.3. Results and discussion

In order to conduct the analysis under a constant displacement magnitude, the structure was excited considering a tip displacement of 110 μm. Moreover, for the sake of investigating the experimental analysis for different values of piezoelectric electromechanical couplings, small capacitors are added in parallel to the piezoelectric element, artificially decreasing the coupling coefficient. Considering such conditions, Fig. 16 shows the harvested power for the SSH-EM, SSHI and standard technique together with the theoretical predictions, when considering an additional capacitor of 0.22 μF in parallel to the piezoelectric transducer. For comparative purposes, the theoretical power when considering the sole use of the electromagnetic transducer has also been plotted. The experimental results demonstrate good agreement with the theoretical analysis, boosting the power gain to a value of 10 compared to the maximum harvested power in the standard interface (20% more compared to the SSHI interface).

However, when it comes to realistic applications, where the system is more likely to be subjected to an external acceleration, one has to keep in mind that extracting energy from mechanical vibrations leads to a reduction of the available mechanical energy due to the harvesting process that yields a mechanical damping effect. This damping effect leads in turn to a power drop, as already
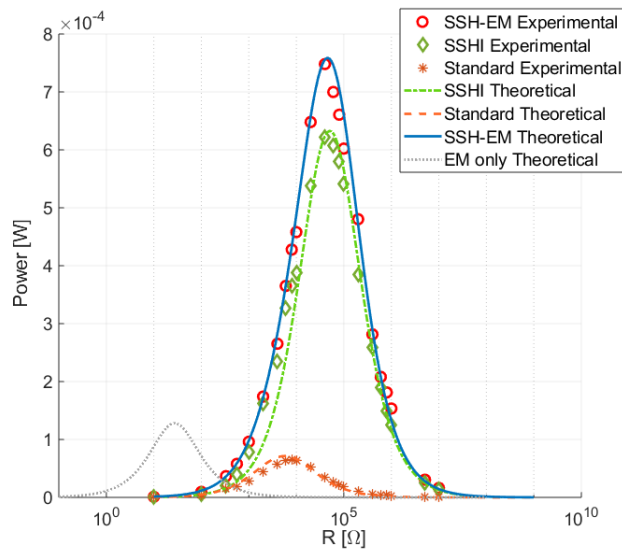

Figure 16: Experimental and theoretical harvested power (considering an additional capacitor of 0.22 µF in parallel with the piezoelectric element) in the constant displacement magnitude case

22

shown theoretically in Fig. 13. Experimental results in this case, along with the theoretical predictions, are depicted Fig. 17, when the structure is driven at resonance frequency under a constant sinusoidal acceleration of 3.8 ms^{-2} (0.39g). As expected, the SSH-EM technique leads to higher harvested power levels for low-coupled systems, while leading to a power drop for higher couplings because of the mutual damping effect between the piezoelectric and electromagnetic transducers. Discrepancies between the experimental results and the theoretical predictions attributed to the diode voltage drop that cannot be longer negligible in low voltage.

6. Conclusion

This paper proposed a nonlinear electric interface applied to a hybrid piezoelectric-electromagnetic energy harvesting system employing the synchronized switch approach derived from the SSHI scheme. Particularly, the proposed technique demonstrated how replacing the passive inductance with an active electromagnetic generator leads to a power enhancement without a particular loss in terms of space. Both theoretical predictions and experimental results have demonstrated that the proposed technique allow boosting the power gain to a factor of 10 when compared to a standard electrical interface, composed of a rectifier bridge and a smoothing capacitor connected to a load, with the possibility of increasing this gain by optimizing the energy conversion capabilities of the electromagnetic transducer.
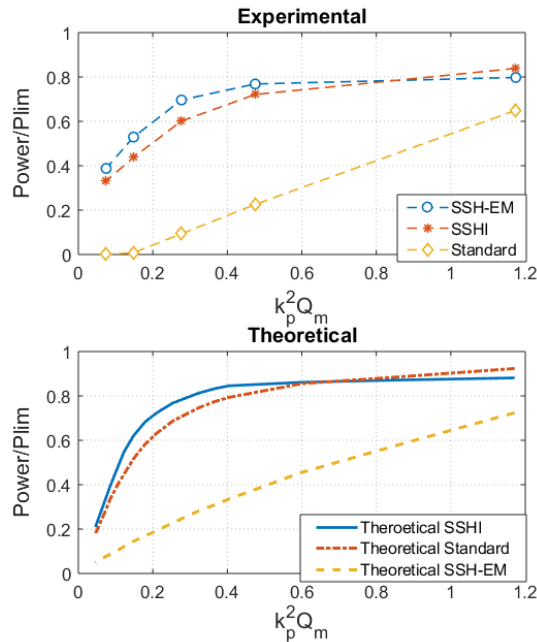

Figure 17: Experimental and theoretical normalized maximum harvested power (w.r.t. the power limit) for each technique versus the squared coupling coefficient and the mechanical quality factor

Appendix .1. Appendix A

The following equation results after the introduction of the normalized terms defined in Eq. (21) and combining Eq. (19), (13) and (5):

$$-\tilde{V} + \tilde{R} - \tilde{R}\tilde{V}\frac{1}{2}\left\{1 - \gamma_0 exp\left[-\frac{1}{2Q_i}\arctan\left(\frac{\beta}{\sqrt{L_0}}\frac{1}{\tilde{V}\frac{\alpha}{\sqrt{C_0}}}\right)\right]\sqrt{\left(\tilde{V}\frac{\alpha}{\sqrt{C_0}}\right)^2 + \left(\frac{\beta}{\sqrt{L_0}}\right)^2}\frac{1}{\tilde{V}\frac{\alpha}{\sqrt{C_0}}}\right\} = 0 \tag{.1}$$

From Eq. (.1), the term $\sqrt{\left(\tilde{V}\frac{\alpha}{\sqrt{C_0}}\right)^2 + \left(\frac{\beta}{\sqrt{L_0}}\right)^2}$ can be approximated by Eq. (.2) (valid for $0 \leq (\beta/\sqrt{L_0})/(\tilde{V}\alpha/\sqrt{C_0}) \leq 1/2$), while the arctangent can be approximated as Eq. (.3) (valid for $-1 \leq (\beta/\sqrt{L_0})/(\tilde{V}\alpha/\sqrt{C_0}) \leq 1$), as demonstrated in [40] and [41], respectively, yielding to Eq. (22).

$$\sqrt{\left(\tilde{V}\frac{\alpha}{\sqrt{C_0}}\right)^2 + \left(\frac{\beta}{\sqrt{L_0}}\right)^2} = \tilde{V}\frac{\alpha}{\sqrt{C_0}} + \frac{\frac{\beta}{\sqrt{L_0}}}{2\tilde{V}\frac{\alpha}{\sqrt{C_0}}} \tag{.2}$$

$$\arctan\left(\frac{\beta}{\sqrt{L_0}}\frac{1}{\tilde{V}\frac{\alpha}{\sqrt{C_0}}}\right) = \frac{\beta}{\sqrt{L_0}}\frac{1}{\tilde{V}\frac{\alpha}{\sqrt{C_0}}}\frac{\pi}{4} \tag{.3}$$

Furthermore, It is known that the explicit solution of the cubic equation $a\tilde{V}^3 + b\tilde{V}^2 + c\tilde{V} + d$ is given by:

$$\tilde{V} = \sqrt[3]{\left(-\frac{b^3}{27a^3} + \frac{bc}{6a^2} - \frac{d}{2a}\right) + \sqrt{\left(-\frac{b^3}{27a^3} + \frac{bc}{6a^2} - \frac{d}{2a}\right)^2 + \left(\frac{c}{3a} - \frac{b}{9a^2}\right)^3}} + $$
$$\sqrt[3]{\left(-\frac{b^3}{27a^3} + \frac{bc}{6a^2} - \frac{d}{2a}\right) - \sqrt{\left(-\frac{b^3}{27a^3} + \frac{bc}{6a^2} - \frac{d}{2a}\right)^2 + \left(\frac{c}{3a} - \frac{b}{9a^2}\right)^3}} - \frac{b}{3a} \tag{.4}$$

However, neglecting the terms $\frac{d}{2a}$ and $\sqrt{\left(-\frac{b^3}{27a^3} + \frac{bc}{6a^2} - \frac{d}{2a}\right)^2 + \left(\frac{c}{3a} - \frac{b}{9a^2}\right)^3}$ (considered to be much smaller than the others) it is possible to obtain an approximated solution of the 3rd order polynomial equation:

$$\tilde{V} = -\frac{b}{3a}\left(1 + 2\sqrt[3]{1 - \frac{9ac}{2b^2}}\right) \tag{.5}$$

Finally, replacing a, b, c with respect to the actual system parameters, leads to Eq. (23).

References

[1] A. Mainwaring, D. Culler, J. Polastre, R. Szewczyk, J. Anderson, Wireless sensor networks for habitat monitoring, in: Proceedings of the 1st ACM international workshop on Wireless sensor networks and applications, Acm, 2002, pp. 88–97.

[2] G. J. Pottie, W. J. Kaiser, Wireless integrated network sensors, Communications of the ACM 43 (5) (2000) 51–58.

[3] C. He, M. E. Kiziroglou, D. C. Yates, E. M. Yeatman, A mems self-powered sensor and rf transmission platform for wsn nodes, IEEE Sensors Journal 11 (12) (2011) 3437–3445.

[4] J. A. Paradiso, T. Starner, Energy scavenging for mobile and wireless electronics, IEEE Pervasive computing (1) (2005) 18–27.

[5] A. Barré, B. Deguilhem, S. Grolleau, M. Gérard, F. Suard, D. Riu, A review on lithium-ion battery ageing mechanisms and estimations for automotive applications, Journal of Power Sources 241 (2013) 680–689.

[6] F. K. Shaikh, S. Zeadally, Energy harvesting in wireless sensor networks: A comprehensive review, Renewable and Sustainable Energy Reviews 55 (2016) 1041–1054.

[7] G. Zhou, L. Huang, W. Li, Z. Zhu, Harvesting ambient environmental energy for wireless sensor networks: a survey, Journal of Sensors 2014 (2014).

[8] S. P. Beeby, M. J. Tudor, N. White, Energy harvesting vibration sources for microsystems applications, Measurement science and technology 17 (12) (2006) R175.

[9] C. Wei, X. Jing, A comprehensive review on vibration energy harvesting: Modelling and realization, Renewable and Sustainable Energy Reviews 74 (2017) 1–18.

[10] H. A. Sodano, D. J. Inman, G. Park, A review of power harvesting from vibration using piezoelectric materials, Shock and Vibration Digest 36 (3) (2004) 197–206.

[11] S. R. Anton, H. A. Sodano, A review of power harvesting using piezoelectric materials (2003–2006), Smart materials and Structures 16 (3) (2007) R1.

[12] C. A. Howells, Piezoelectric energy harvesting, Energy Conversion and Management 50 (7) (2009) 1847–1850.

[13] I. Izadgoshasb, Y. Y. Lim, L. Tang, R. V. Padilla, Z. S. Tang, M. Sedighi, Improving efficiency of piezoelectric based energy harvesting from human motions using double pendulum system, Energy conversion and management 184 (2019) 559–570.

[14] T. Kashiwao, I. Izadgoshasb, Y. Y. Lim, M. Deguchi, Optimization of rectifier circuits for a vibration energy harvesting system using a macro-fiber composite piezoelectric element, Microelectronics Journal 54 (2016) 109–115.

[15] I. Izadgoshasb, Y. Y. Lim, R. Vasquez Padilla, M. Sedighi, J. P. Novak, Performance enhancement of a multiresonant piezoelectric energy harvester for low frequency vibrations, Energies 12 (14) (2019) 2770.

[16] S. P. Beeby, R. Torah, M. Tudor, P. Glynne-Jones, T. O'donnell, C. Saha, S. Roy, A micro electromagnetic generator for vibration energy harvesting, Journal of Micromechanics and microengineering 17 (7) (2007) 1257.

[17] E. Arroyo, A. Badel, F. Formosa, Energy harvesting from ambient vibrations: Electromagnetic device and synchronous extraction circuit, Journal of Intelligent Material Systems and Structures 24 (16) (2013) 2023–2035.

[18] C. Saha, T. O'donnell, N. Wang, P. McCloskey, Electromagnetic generator for harvesting energy from human motion, Sensors and Actuators A: Physical 147 (1) (2008) 248–253.

[19] A. R. M. Siddique, S. Mahmud, B. Van Heyst, A comprehensive review on vibration based micro power generators using electromagnetic and piezoelectric transducer mechanisms, Energy Conversion and Management 106 (2015) 728–747.

[20] E. Lefeuvre, A. Badel, C. Richard, L. Petit, D. Guyomar, A comparison between several vibration-powered piezoelectric generators for standalone systems, Sensors and Actuators A: Physical 126 (2) (2006) 405–416.

[21] M. Lallart, Nonlinear technique and self-powered circuit for efficient piezoelectric energy harvesting under unloaded cases, Energy conversion and management 133 (2017) 444–457.

[22] D. Guyomar, M. Lallart, Recent progress in piezoelectric conversion and energy harvesting using nonlinear electronic interfaces and issues in small scale implementation, Micromachines 2 (2) (2011) 274–294.

[23] D. Guyomar, A. Badel, E. Lefeuvre, C. Richard, Toward energy harvesting using active materials and conversion improvement by nonlinear processing, IEEE transactions on ultrasonics, ferroelectrics, and frequency control 52 (4) (2005) 584–595.

[24] M. Lallart, L. Garbuio, L. Petit, C. Richard, D. Guyomar, Double synchronized switch harvesting (dssh): A new energy harvesting scheme for efficient energy extraction, IEEE transactions on ultrasonics, ferroelectrics, and frequency control 55 (10) (2008) 2119–2130.

[25] M. Lallart, D. Guyomar, Piezoelectric conversion and energy harvesting enhancement by initial energy injection, Applied Physics Letters 97 (1) (2010) 014104.

26

[26] L. Garbuio, M. Lallart, D. Guyomar, C. Richard, D. Audigier, Mechanical energy harvester with ultralow threshold rectification based on sshi nonlinear technique, IEEE Transactions on Industrial Electronics 56 (4) (2009) 1048–1056.

[27] M. Lallart, W.-J. Wu, Y. Hsieh, L. Yan, Synchronous inversion and charge extraction (sice): a hybrid switching interface for efficient vibrational energy harvesting, Smart Materials and Structures 26 (11) (2017) 115012.

[28] M. Lallart, C. Magnet, C. Richard, E. Lefeuvre, L. Petit, D. Guyomar, F. Bouillault, New synchronized switch damping methods using dual transformations, Sensors and Actuators A: Physical 143 (2) (2008) 302–314.

[29] E. Arroyo, A. Badel, Electromagnetic vibration energy harvesting device optimization by synchronous energy extraction, Sensors and Actuators A: Physical 171 (2) (2011) 266–273.

[30] M. Lallart, D. J. Inman, Mechanical effect of combined piezoelectric and electromagnetic energy harvesting, in: Structural Dynamics and Renewable Energy, Volume 1, Springer, 2011, pp. 261–272.

[31] S. Zolfaghar Tehrani, H. Ranjbar, P. Vial, P. Premaratne, A New Efficient Power Management Interface for Hybrid Electromagnetic-Piezoelectric Energy Harvesting System, 2019, pp. 537–542. doi:10.1007/978-3-030-14070-0_75.

[32] H. Xia, R. Chen, L. Ren, Analysis of piezoelectric–electromagnetic hybrid vibration energy harvester under different electrical boundary conditions, Sensors and Actuators A: Physical 234 (2015) 87–98.

[33] H. Liu, S. Gao, J. Wu, P. Li, Study on the output performance of a nonlinear hybrid piezoelectric-electromagnetic harvester under harmonic excitation, in: Acoustics, Vol. 1, Multidisciplinary Digital Publishing Institute, 2019, pp. 382–392.

[34] T. Wacharasindhu, J. Kwon, A micromachined energy harvester from a keyboard using combined electromagnetic and piezoelectric conversion, Journal of Micromechanics and Microengineering 18 (10) (2008) 104016.

[35] R. Toyabur, M. Salauddin, H. Cho, J. Y. Park, A multimodal hybrid energy harvester based on piezoelectric-electromagnetic mechanisms for low-frequency ambient vibrations, Energy Conversion and Management 168 (2018) 454–466.

[36] M. Rajarathinam, S. Ali, Energy generation in a hybrid harvester under harmonic excitation, Energy Conversion and Management 155 (2018) 10–19.

[37] A. Badel, F. Formosa, M. Lallart, Electromechanical transducers (2015).

[38] C. Williams, R. B. Yates, Analysis of a micro-electric generator for microsystems, sensors and actuators A: Physical 52 (1-3) (1996) 8–11.

[39] E. Arroyo, A. Badel, F. Formosa, Y. Wu, J. Qiu, Comparison of electromagnetic and piezoelectric vibration energy harvesters: Model and experiments, Sensors and Actuators A: Physical 183 (2012) 148–156.

[40] S. D. Roy, Approximating the square root of the sum of two squares, IETE Journal of Education 32 (2) (1991) 11–13.

[41] S. Rajan, S. Wang, R. Inkol, A. Joyal, Efficient approximations for the arctangent function, IEEE Signal Processing Magazine 23 (3) (2006) 108–111.